A General Pressure Gradient Formulation for Ocean Models

Part II: Energy, Momentum, and Bottom Torque Consistency

Y. Tony Song

Earth and Space Sciences Division

Jet Propulsion Laboratory

California Institute of Technology

Pasadena, CA 91109

Daniel G. Wright

Fisheries and Oceans Canada, Bedford Institute of Oceanography

Dartmouth, Nova Scotia, CANADA B2Y 4A2

Abstract

A new formulation of the pressure gradient force for use in models with topography-following coordinates is proposed and diagnostically analyzed by Song (this issue). Here, we show that important properties of the continuous equations are retained by the resulting numerical schemes, and we examine their performance in prognostic simulations. We investigate numerical consistency with respect to global energy conservation, depth-integrated momentum changes, and the represent of the bottom pressure torque. The performances of the numerical schemes are tested in prognostic integrations of an ocean model to demonstrate numerical accuracy and long-term integral stability. Two typical geometries, an isolated tall seamount and an unforced basin with sloping boundaries, are considered for the special case of no external forcing and horizontal isopycnals to test numerical accuracy. These test problems confirm that the proposed schemes yield accurate approximations to the pressure gradient force. Integral consistency conditions are verified and the energetics of the "advective elimination" of the pressure gradient error (Mellor et al., 1994) is considered.

A large-scale wind-driven basin with and without topography is used to test the model's long-term integral performance and the effects of bottom pressure torque on the transport in western boundary currents. Integrations are carried out for 10 years in each case and results show that the schemes are stable, and the steep topography causes no obvious numerical problems. A realistic meandering western boundary current is well developed with detached cold cyclonic and warm anticyclonic eddies as it extends across the basin. In addition, the results with topography show earlier separation and enhanced transport in the western boundary currents due to the bottom pressure torque.

1

1   Introduction

The importance of the ocean's bathymetry in controlling both large and small scale ocean circulation patterns is apparent. Motivated by this fact, modelers have used various topography-following coordinates in order to better resolve the ocean's bathymetry (Blumberg and Mellor 1987, Gerdes 1993, Simmons and Burridge 1981, Song and Haidvogel 1994). Unfortunately, errors in the pressure gradient force have been associated with the use of these coordinates, and since both the major ocean currents and eddies are in approximate geostrophic balance, such errors are clearly a concern (Haney 1991). In part I, Song (this issue) proposed a generalized pressure gradient formulation, and considered two specific formulations which can reduce the pressure gradient errors in numerical ocean models. Truncation errors have been analytically examined and diagnostically evaluated in several test cases. However, their performances in prognostic integrations of ocean models have not been tested.

It is certainly desirable to minimize errors in numerical schemes, but some truncation error will always exist in a model with finite resolution. Many schemes share the same order of accuracy, but their solutions approach the true solution along different paths in function space. Thus, for any finite resolution, the net effect of truncation error will depend on factors other than just resolution. In particular, integral properties of the discrete scheme could play an important role in constraining model errors, and discrete schemes are often designed so that the solutions approach the true solution along a path on which desirable integral properties are maintained (Bryan, 1969; Arakawa and Lamb, 1977; Arakawa and Suarez, 1983; Arakawa and Konor, 1996). A scheme which retains integral properties of the continuous equations is said to be discrete consistent with respect to these properties.

In this contribution, we examine whether or not certain important integral properties of the continuous equations are retained by the proposed schemes and we examine their performance in prognostic model simulations. The properties considered are the conservation of total energy and momentum, and the accurate representation of the bottom pressure torque. To evaluate the accuracy of the schemes, we consider two test problems. The first examines errors

associated with an isolated tall seamount in an otherwise flat-bottomed basin (Beckmann and Haidvogel, 1993; Yingshuo and Thompson, 1997), and the second considers the errors associated with sloping boundaries around a flat-bottomed basin (Mellor et al., 1994; hereafter referred to as MEO). We also use these two test problems to verify our theoretical conclusions regarding momentum and energetic consistency.

Bottom topography has long been recognized as an important factor in the determination of the path of western boundary currents. For example, Holland (1967, 1973) shows that the presence of sloping topography leads to earlier separation of the western boundary currents and enhanced transport of the anticyclonic subtropical gyre with respect to the Sverdrup transport. Major differences are attributed to the joint effect of baroclinicity and relief (JEBAR), an important component of the bottom pressure torque (Greatbatch et al. 1991; Mertz and Wright, 1992; Myers et al., 1995). To examine the performance of the pressure gradient schemes in long-term, large-scale ocean modeling and to verify model robustness in a case where the bottom pressure torque is significant, we consider two classical problems in oceanography: the adiabatic, wind-driven, time-averaged circulation in a mid-latitude rectangular basin, first with a flat bottom and then with sloping topography on the west side of the basin. The model is run for 10 years in each case to reach a well-developed stage including a strong western boundary current and detached eddies. The presence of topography leads to significantly earlier separation of the boundary current and enhanced transport within the basin due to JEBAR.

In the following section we show that the proposed discrete schemes conserve the basin-integrated energy. The vertically integrated momentum along a closed bottom contour is not represented exactly, but the errors are shown to be very small. The accurate representation of JEBAR effects by the present model formulation is also demonstrated analytically. The conservation properties are verified in section 3 by examining two specific examples. In section 4, the numerical stability of the model during long term integrations, with and without topography, is illustrated through examples. Final discussion and conclusions are given in section 5.

2 Discrete Consistency

In this section, we focus attention on the integral properties of the proposed schemes. Similar integral properties are considered by Arakawa and Konor (1996) in their hybrid $\sigma - p$ coordinates with the Charney-Phillips grid. Arakawa and Suarez (1983) state that, of the four integral conditions considered Arakawa and Lamb (1977), they regard the two constraints dealing with the pressure gradient force as most important. These are:

(A) Energetic Consistency: The finite-difference analogue of the energy conversion term must have the same form in the kinetic energy and thermodynamic equations, and

(B) Momentum Consistency: The pressure gradient force must not generate vertically integrated circulation along a contour of constant bottom pressure.

In addition, we show that the pressure gradient formulation results in a consistent representation of the bottom pressure torque, i.e.,

(C) Bottom Torque Consistency: The pressure gradient scheme conserves the curl of the vertically integrated pressure gradient force.

These measures of integral consistency are considered below by comparing the continuous forms to their finite-difference analogues in the s-coordinate system. The derivations are based on a numerical scheme using an Arakawa C-grid in the horizontal and staggered vertical levels as shown in Fig. 1 of Part I. To examine these consistency conditions, we will use the following notations

$$\nabla_z = (\frac{\partial}{\partial x}, \frac{\partial}{\partial y})|_z \ ,$$
$$\nabla = (\frac{\partial}{\partial x}, \frac{\partial}{\partial y})|_s \ ,$$
$$\delta_x b_{i+\frac{1}{2}} = b_{i+1} - b_i \ ,$$
$$\overline{b}^x_{i+\frac{1}{2}} = \frac{1}{2}(b_{i+1} + b_i) \ , \tag{2.1}$$

and the relations

$$a\delta_x b = \delta_x(\overline{a}^x b) - \overline{b\delta_x a}^x \ ,$$

3

$$\overline{a}^x \delta_x b = \delta_x(ab) - \overline{b}^x \delta_x a \quad,$$

$$\delta_x \delta_s b = \delta_s \delta_x b \quad, \tag{2.2}$$

where the subscripts z and s indicate that the gradients are taken along surfaces of constant z and s, respectively. z is the vertical coordinate in a Cartesian coordinate system and s is a general vertical coordinate, such as the generalized topography-following coordinate system considered by Song and Haidvogel (1994). Analogous notations and relations also apply for the y and z directions.

In Part I, Song (this issue) discussed two schemes for the pressure gradient force, the standard and weighted Jacobian schemes. In this section, we will focus on the standard scheme based on a Jacobian formulation in which

$$PX_k = PX_\zeta - \sum_{k'=k}^{K} \delta \mathcal{J}_{k'+\frac{1}{2}}, \tag{2.3}$$

where

$$\delta \mathcal{J}_{k+\frac{1}{2}} = \left(\delta_s \overline{z}^x \delta_x \overline{b}^s - \delta_x \overline{z}^s \delta_s \overline{b}^x \right)_{k+\frac{1}{2}} \quad, \tag{2.4}$$

$\zeta = \zeta(x, y, t)$ is the sea surface elevation and $b = -g\rho/\rho_0$ is the buoyancy. The formulation is based on the Arakawa C-grid in the horizontal and a staggered grid in the vertical, as given in Fig. 1 of Part I. $z_{K+\frac{1}{2}}$ is at the sea surface $z = \zeta$, $z_{\frac{1}{2}}$ is at the bottom $z = -h$, and $\delta_s z_k = z_{k+\frac{1}{2}} - z_{k-\frac{1}{2}}$. Using the last two relations in (2.1), we have the following equivalent conservation form

$$\delta J_{k+\frac{1}{2}} = \delta_x (\overline{b}^s \delta_s z)_{k+\frac{1}{2}} - \delta_s (\overline{b}^x \delta_x z)_{k+\frac{1}{2}} \quad, \tag{2.5}$$

which is useful for the derivations of the integral consistency conditions. Using the conservation form, our numerical scheme for the pressure difference at the kth-level of the s-coordinate can be written as

$$PX_k = PX_\zeta - \sum_{k'=k}^{K} \left\{ \delta_x (\overline{b}^s \delta_s z) - \delta_s (\overline{b}^x \delta_x z) \right\}_{k'+\frac{1}{2}}, \tag{2.6}$$

$$PY_k = PY_\zeta - \sum_{k'=k}^{K} \left\{ \delta_y (\overline{b}^s \delta_s z) - \delta_s (\overline{b}^y \delta_y z) \right\}_{k'+\frac{1}{2}}, \tag{2.7}$$

4

in the x- and y-direction, respectively. For simplicity, in the following derivations we consider $PX_\zeta = PY_\zeta = 0$, and δx and δy are assumed uniform in both x and y directions.

2.1 Energetic Consistency

The hydrostatic, Boussinesq primitive equations in the z-system can be written as

$$\frac{\partial \mathbf{u}}{\partial t} + \mathbf{u} \cdot \nabla_z \mathbf{u} + w \frac{\partial \mathbf{u}}{\partial z} + \mathbf{f} \times \mathbf{u} + \frac{1}{\rho_0} \nabla_z P = \mathbf{F}, \tag{2.8}$$

$$\frac{\partial \rho}{\partial t} + \mathbf{u} \cdot \nabla_z \rho + w \frac{\partial \rho}{\partial z} = Q, \tag{2.9}$$

$$\frac{\partial p}{\partial z} + g\rho = 0, \tag{2.10}$$

$$\nabla_z \cdot \mathbf{u} + w_z = 0. \tag{2.11}$$

The corresponding equations in the s-system are (Song and Haidvogel, 1994)

$$\frac{D}{Dt}\left(\frac{\partial z}{\partial s}\mathbf{u}\right) + \frac{\partial z}{\partial s}\mathbf{f} \times \mathbf{u} - \frac{\partial z}{\partial s}\int_s^0 \left\{\frac{\partial z}{\partial s}\nabla b - \frac{\partial b}{\partial s}\nabla z\right\} = \frac{\partial z}{\partial s}\mathbf{F}, \tag{2.12}$$

$$\frac{D}{Dt}\left(\frac{\partial z}{\partial s}\rho\right) = \frac{\partial z}{\partial s}Q, \tag{2.13}$$

$$\frac{\partial p}{\partial s} + \frac{\partial z}{\partial s}g\rho = 0, \tag{2.14}$$

$$\nabla \cdot \left(\frac{\partial z}{\partial s}\mathbf{u}\right) + \frac{\partial \omega}{\partial s} = 0, \tag{2.15}$$

where

$$\frac{D*}{Dt} = \frac{\partial *}{\partial t} + \nabla \cdot \left(\frac{\partial z}{\partial s}\mathbf{u}*\right) + \frac{\partial(\omega *)}{\partial s}, \tag{2.16}$$

and $\omega = w - \mathbf{u} \cdot \nabla z$ is the vertical velocity in the s-system.

These equations have kinetic energy density (**KE**) of $\mathbf{u} \cdot \mathbf{u}/2$ and potential energy density (**PE**) of $-zg\rho/\rho_0 = zb$ (Gent, 1993). Taking the dot product of (2.12) with $\mathbf{u}$ and multiplying (2.13) by gz/ρ_0 and using (2.15) we obtain

$$\frac{D}{Dt}\left(\frac{\partial z}{\partial s}\mathbf{KE}\right) = \frac{\partial z}{\partial s}\mathbf{u} \cdot \int_s^0 \left\{\frac{\partial z}{\partial s}\nabla b - \frac{\partial b}{\partial s}\nabla z\right\} ds + \frac{\partial z}{\partial s}\mathbf{u} \cdot \mathbf{F}, \tag{2.17}$$

$$\frac{D}{Dt}\left(\frac{\partial z}{\partial s}\mathbf{PE}\right) = -\frac{\partial z}{\partial s}b\{\omega + \mathbf{u} \cdot \nabla z\} + \frac{\partial z}{\partial s}\frac{gz}{\rho_0}Q. \tag{2.18}$$

The rate of kinetic energy generated by the pressure gradient force is thus

$$\frac{\partial z}{\partial s}\mathbf{u} \cdot \int_s^0 \left\{\frac{\partial z}{\partial s}\nabla b - \frac{\partial b}{\partial s}\nabla z\right\} ds$$

$$= \frac{\partial z}{\partial s} \mathbf{u} \cdot \int_s^0 \left\{ \nabla \left(\frac{\partial z}{\partial s} b \right) - \frac{\partial}{\partial s} \left(b \nabla z \right) \right\} ds$$

$$= \nabla \cdot \left\{ \frac{\partial z}{\partial s} \mathbf{u} \int_s^0 \frac{\partial z}{\partial s} b ds \right\} - \nabla \left(\frac{\partial z}{\partial s} \mathbf{u} \right) \int_s^0 \frac{\partial z}{\partial s} b ds + b \frac{\partial z}{\partial s} \mathbf{u} \cdot \nabla z$$

$$= \nabla \cdot \left(\frac{\partial z}{\partial s} \mathbf{u} \int_s^0 \frac{\partial z}{\partial s} b ds \right) + \frac{\partial}{\partial s} \left(\omega \int_s^0 \frac{\partial z}{\partial s} b ds \right) + \frac{\partial z}{\partial s} b \left\{ \omega + \mathbf{u} \cdot \nabla z \right\} \quad . \qquad (2.19)$$

Substituting into the **KE** equation and combining with the **PE** equation, we have the total energy equation:

$$\frac{D}{Dt} \left(\frac{\partial z}{\partial s} [\mathbf{KE} + \mathbf{PE}] \right) = \nabla \left(\frac{\partial z}{\partial s} \mathbf{u} \int_s^0 \frac{\partial z}{\partial s} b ds \right) + \frac{\partial}{\partial s} \left(\omega \int_s^0 \frac{\partial z}{\partial s} b ds \right) + \frac{\partial z}{\partial s} \left\{ \mathbf{u} \cdot \mathbf{F} + \frac{g}{\rho_0} Q \right\}.$$
$$(2.20)$$

Integrating over the entire domain and applying conditions of no normal flow through solid boundaries gives the conservation of total energy when $\mathbf{F} = 0$ and $Q = 0$.

$$\frac{D}{Dt} \int \int_\Omega \int_{-1}^0 \frac{\partial z}{\partial s} [\mathbf{KE} + \mathbf{PE}] ds d\Omega = \frac{D}{Dt} < \mathbf{KE} + \mathbf{PE} >= 0, \qquad (2.21)$$

where the pair of angle brackets $<>$ indicates domain integration. Conservation of total energy in the discrete scheme can be shown following Bleck (1978) or Arakawa and Lamb (1978). Below, we discuss only the consistency of the energy conversions related to the pressure gradient (i.e., the first term on the right sides of (2.17) and (2.18)).

First, consider the contribution of the pressure gradient force to the kinetic energy equation. This contribution arises from the first term on the right side of (2.17) which, for the continuous equations, can be rewritten in the form (2.19). We use the form (2.6) to write the integral over x of the contribution from the x-direction as

$$\sum_{i=1}^L \delta_s \bar{z}_{i-\frac{1}{2}}^x u \left\{ \delta_x \left(\sum_{k'=k}^K \bar{b}^s \delta_s z_{k'+\frac{1}{2}} \right) + \bar{b}^x \delta_x z_k \right\}_{i-\frac{1}{2}} . \qquad (2.22)$$

Using the sum-by-parts relation, $\sum_{i=1}^L a_{i-\frac{1}{2}} \delta_x b_{i-\frac{1}{2}} = a_{L+\frac{1}{2}} b_L - a_{\frac{1}{2}} b_0 - \sum_{i=1}^L b_i \delta_x a_i$, the first term in (2.22) can be written as

$$-\sum_{i=1}^L \left\{ \delta_x (\delta_s \bar{z}^x u) \sum_{k'=k}^K \bar{b}^s \delta_s z_{k'+\frac{1}{2}} \right\}_i , \qquad (2.23)$$

since u vanishes at both ends for no normal flux conditions. The no flux boundary condition also allows us to write the second term in (2.22) as

$$\sum_{i=1}^{L} \overline{\left\{ \delta_s \bar{z}_k^x u \bar{b}^x \delta_x z_k \right\}}^x_i .$$

(2.24)

Similarly, from the y-direction, we obtain the contribution

$$-\sum_{j=1}^{M} \left\{ \delta_y (\delta_s \bar{z}^y v) \sum_{k'=k}^{K} \bar{b}^s \delta_s z_{k'+\frac{1}{2}} - \overline{\delta_s \bar{z}_k^x v \bar{b}^y \delta_y z_k}^y \right\}_j .$$

(2.25)

Using the continuity equation, the first terms in (2.22) and (2.25) can be combined and rewritten as follows.

$$-\sum_{k=1}^{K}\sum_{j=1}^{M}\sum_{i=1}^{L} \left\{ \delta_x \left(\delta_s \bar{z}^x u \right) + \delta_y \left(\delta_s \bar{z}^y v \right) \right\} \sum_{k'=k}^{K} \bar{b}^s \delta_s z_{k'+\frac{1}{2}} = \sum_{k=1}^{K}\sum_{j=1}^{M}\sum_{i=1}^{L} \left\{ \delta_s \omega \sum_{k'=k}^{K} \bar{b}^s \delta_s z_{k'+\frac{1}{2}} \right\}$$

$$= \sum_{k=1}^{K}\sum_{j=1}^{M}\sum_{i=1}^{L} \left\{ \overline{\omega \bar{b}^s \delta_s z}^s \right\}_{i,j,k} .$$

(2.26)

Notice that the relation (2.2a), applied in the vertical direction, is used in the last step of the derivation. Finally, adding (2.24)-(2.25) and using (2.26) gives

$$\sum_{k=1}^{K}\sum_{j=1}^{M}\sum_{i=1}^{L} \left\{ \overline{\omega \bar{b}^s \delta_s z}^s + \overline{\delta_s \bar{z}^x u \bar{b}^x \delta_x z}^x + \overline{\delta_s \bar{z}^x v \bar{b}^y \delta_y z}^y \right\}_{i,j,k} .$$

(2.27)

It is now easily shown that the first term on the right side of (2.18) yields the negative of this expression, as required for energetic consistency.

2.2 Momentum Consistency

Conservation of momentum requires that the pressure gradient force generates no vertically integrated circulation along a closed bottom pressure contour, i.e., a contour of $p_b = p_s - \int_{-h}^{0} b\,dz$, where $p = P/\rho_0$ is the dynamic pressure. To show that this is satisfied for the continuous system, we first write the pressure gradient as:

$$\nabla_z p = \nabla p - b \nabla z .$$

(2.28)

Vertical integration gives

$$\int_{-h}^{\zeta} (\nabla_z p) dz = \int_{-1}^{0} (\nabla p - b \nabla z) \frac{\partial z}{\partial s} ds$$

$$
\begin{aligned}
&= \nabla \int_{-1}^{0} \frac{\partial z}{\partial s} p \, ds - \int_{-1}^{0} \left\{ p \nabla \left(\frac{\partial z}{\partial s} \right) + \frac{\partial z}{\partial s} b \nabla z \right\} ds \\
&= \nabla \int_{-1}^{0} \frac{\partial z}{\partial s} p \, ds - \int_{-1}^{0} \frac{\partial}{\partial s} \left[p \nabla z \right] ds \\
&= \nabla \left\{ \int_{-1}^{0} \frac{\partial z}{\partial s} p \, ds \right\} - p_b \nabla h \quad .
\end{aligned}
\tag{2.29}
$$

The line integral of the tangential component of the gradient vector, taken along an arbitrary closed curve, vanishes. Along contours of constant bottom pressure, p_b, or bottom depth, h, the second term also vanishes. Thus the pressure gradient force conserves momentum along closed contours of either p_b or h.

Now we want to show that our numerical scheme retains this property in its discrete form. First, using the scheme given in equation (2.6), the vertically integrated discrete pressure gradient in the x-direction is given by

$$
\begin{aligned}
\sum_{k=1}^{K} \delta_s \bar{z}_k^x P X_k &= - \sum_{k=1}^{K} \left\{ \delta_s \bar{z}_k^x \sum_{k'=k}^{K} \delta_x (\bar{b}^s \delta_s z)_{k'+\frac{1}{2}} + \delta_s \bar{z}_k^x (\bar{b}^x \delta_x z)_k \right\} \\
&= - \sum_{k=1}^{K} \left\{ \delta_s \bar{z}_k^x \delta_x \left(\sum_{k'=k}^{K} \bar{b}^s \delta_s z_{k'+\frac{1}{2}} \right) - \delta_s \left(\sum_{k'=k}^{K} \bar{b}^x \delta_s \bar{z}_{k'}^x \right) \delta_x z_k \right\} .
\end{aligned}
\tag{2.30}
$$

The two bracketed sums represent estimates of the pressures at grid points (i, k) and $(i + \frac{1}{2}, k - \frac{1}{2})$, which we represent by

$$
\hat{p}_{i,k}^s = - \sum_{k'=k}^{K} (\bar{b}^s \delta_s z)_{i,k'+\frac{1}{2}}
\tag{2.31}
$$

and

$$
\hat{p}_{i+\frac{1}{2},k-\frac{1}{2}}^x = - \sum_{k'=k}^{K} (\bar{b}^x \delta_s \bar{z}^x)_{i+\frac{1}{2},k'} \quad ,
\tag{2.32}
$$

respectively. It should be noted that $\hat{p}^s$ and $\hat{p}^x$ are not necessarily equal to

$$
\bar{p}_{i,k}^s = \frac{1}{2} (p_{i,k-\frac{1}{2}} + p_{i,k+\frac{1}{2}})
\tag{2.33}
$$

and

$$
\bar{p}_{i+\frac{1}{2},k-\frac{1}{2}}^x = \frac{1}{2} (p_{i,k-\frac{1}{2}} + p_{i+1,k-\frac{1}{2}}) \quad ,
\tag{2.34}
$$

respectively, even though they are similarly staggered relative to $p_{i,k+\frac{1}{2}}$ which is the pressure at locations $(i, k + \frac{1}{2})$.

8

Substituting (2.31)-(2.32) into equation (2.30) and using the notation $z_k = \bar{z}^s$, we have

$$\sum_{k=1}^{K} \left\{ \delta_s \bar{z}^x \delta_x \hat{p}^s - \delta_s \hat{p}^x \delta_x \bar{z}^s \right\}$$

$$= \sum_{k=1}^{K} \left\{ \delta_x (\hat{p}^s \delta_s z) - \delta_s (\hat{p}^x \delta_x z) \right\} - \hat{p}'_b \delta_x h$$

$$= \delta_x \left\{ \sum_{k=1}^{K} \hat{p}^s \delta_s z \right\} - (\hat{p}^x_b + \hat{p}'_b) \delta_x h \tag{2.35}$$

where

$$\hat{p}'_b = \sum_{k=1}^{K} \left(\overline{\hat{p}^s}^x - \overline{\hat{p}^x}^s \right) \delta_x \delta_s z / \delta_x h \quad . \tag{2.36}$$

Note that $\delta_x \delta_s z \leq \delta_x h$ so that $\hat{p}'_b = 0$ is well-defined even over a flat bottom. It should also be noted that this might be a problem in cases where the slope of the vertical levels may be greater than the bottom slope, such as in the isopycnal coordinate system or in an unstructured vertical grid.

The quantity $\hat{p}^x_b$ is the bottom pressure at the locations where $\hat{p}^x$ is determined by (2.32), and $\hat{p}'_b$ is a correction to this pressure required for consistency with the integrated bottom torque along a closed bottom pressure contour. If we define

$$\overline{p}^x_b = \hat{p}^x_b + \hat{p}'_b \tag{2.37}$$

along the contour, where the x indicates the direction of the contour line from one ρ point to any adjacent ρ point and the overbar indicates the midpoint, then (2.35) becomes

$$\delta_x \left\{ \sum_{k=1}^{K} \hat{p}^s \delta_s z \right\} - \overline{p}^x_b \delta_x h \quad . \tag{2.38}$$

Clearly, (2.38) is analogous to the continuous equation (2.29), i.e., the pressure gradient force generates no vertically integrated circulation when integrated around a contour of constant bottom pressure, or along a contour of constant depth. In the next section, we will test the accuracy of this consistency relation for the closed contours surrounding a seamount.

The integral consistencies discussed above suggest that the numerical scheme will yield consistent large scale properties when used in longterm integrations. Obviously, it is also

highly desirable for a numerical scheme to give an accurate representation of the local circulation. If we consider that thermal wind dominates the vertical structure and that this is easily represented, then it follows that it is most critical to ensure that the vertically averaged equations are accurately represented. If a vorticity equation for the depth integrated flow is formed (e.g., Holland, 1973; Mertz and Wright, 1992), then the importance of the bottom pressure torque is immediately obvious. The discrete representation of this term is discussed below.

2.3 Bottom Torque Consistency

Accurate representation of the bottom pressure torque, $J(p_b, h)$ (Sarkisyan and Ivanov (1971)), is critical for many oceanographic applications. For example, it is a key part of the vorticity balance required to obtain a realistic circulation in the North Atlantic ocean (Holland 1973, Greatbatch et al. 1991, Myers et al. 1995). One component of this torque, which has received much attention because of its importance, is the joint effect of baroclinicity and relief (JEBAR), which represents a correction to the topographic stretching term to account for the fact that the bottom velocity rather than the depth-averaged flow provides the vortex stretching (Mertz and Wright, 1992). Diagnostic calculations such as those presented by Mellor et al. (1982), and the previous studies discussed therein, clearly illustrate both the difficulty and the importance of accurately representing this term.

Beckmann and Haidvogel (1993) show that the original pressure gradient scheme (OPG) based on equation (1.1) does not accurately represent the bottom torque. They present a modified scheme which is shown to guarantee the correct representation of this effect, but the resulting scheme generally has larger local error than the OPG. Here, we show that the formulation of the pressure gradient force discussed in Part I retains the correct bottom pressure torque.

From equation (2.29), the vertically integrated pressure gradient force can be written as

$$-\int_{-h}^{0} \nabla_z p \, dz = -\nabla \left\{ \int_{-1}^{0} \frac{\partial z}{\partial s} p \, ds \right\} - p_b \nabla h, \qquad (2.39)$$

and the bottom pressure torque, which results from taking the curl of the vertically integrated

pressure gradient force, is given by

$$J(p_b, h) = \frac{\partial}{\partial x}\left(p_b \frac{\partial h}{\partial y}\right) - \frac{\partial}{\partial y}\left(p_b \frac{\partial h}{\partial x}\right) = \frac{\partial p_b}{\partial x}\frac{\partial h}{\partial y} - \frac{\partial p_b}{\partial y}\frac{\partial h}{\partial x}. \qquad (2.40)$$

Similarly, from (2.38), the discrete form of the integrated pressure gradient force in the x-direction can be written as

$$-\sum_{k=1}^{K} \delta_s \bar{z}^x\, PX_k = -\delta_x\left\{\sum_{k=1}^{K} \delta_s z\, p_k\right\} - \bar{p}_b^x \delta_x h \quad, \qquad (2.41)$$

and in the y-direction as

$$-\sum_{k=1}^{K} \delta_s \bar{z}^y\, PY_k = -\delta_y\left\{\sum_{k=1}^{K} \delta_s z\, p_k - h p_b\right\} - \bar{p}_b^y \delta_y h \quad. \qquad (2.42)$$

The curl of these expressions,

$$\delta_x\left(\overline{p_b}^y \delta_y h\right) - \delta_y\left(\overline{p_b}^x \delta_x h\right) \quad, \qquad (2.43)$$

gives the analogous form of (2.40). Thus the bottom pressure torque is accurately represented without requiring any modifications of our numerical scheme.

In the remainder of this study, we examine several particular ocean modeling problems which provide further evidence of the utility of these schemes in prognostic integrations. These problems will also be used to verify the integral consistency relations discussed in this section.

3   Performance in Unforced Examples

In this section, we consider two problems in order to evaluate the performance of the pressure gradient schemes in the S-Coordinate Rutgers University Model (SCRUM, Song and Haidvogel 1994, Song 1996) in highly idealized situations for which the exact solution is known. The primary differences from the examples of Part I are that the density field evolves prognostically with time and the calculations are 3-dimensional rather than 2-dimensional. The test problems follow Beckman and Haidvogel (1993) and Mellor et al. (1994) to evaluate model errors associated with a tall seamount and continental slopes, respectively. Both problems are unforced so that the effects of pressure gradient errors can be easily evaluated.

3.1 An Isolated Seamount

The seamount test case provides a measure of the errors in the pressure gradient term in the presence of steep topography and can be directly compared to the results of Beckmann and Haidvogel (1993) and McCalpin (1995). The configuration is a tall, steep seamount in a channel, closed to the north and south and recirculating through the east and west boundaries. The computational domain has dimensions of approximately 320 km by 320 km, and is divided into 40×40 grid cells. The isolated seamount is located in the center of the channel and its topography is described by a Gaussian profile

$$h(x, y) = 5000 - 4500 e^{-(r/l)^2},$$

where $r = \sqrt{(x - x_c)^2 + (y - y_c)^2}$ is the distance from the center of the domain and $l = 40$ km is the width of the seamount. By using an unevenly spaced horizontal grid, finer resolution is achieved near the center of the domain with a 2:1 variation in grid spacing from the center to the edges. The enhancement is applied in the same manner in both the x and y directions. The maximum values of slope and $|(\delta_x h)/h|$ are about 0.096 and 0.35, respectively. Hydrostatic consistency is violated with the maximum value of $|(s\delta_x h)/h\delta s|$ being about 7 with 20 evenly spaced vertical levels.

The stratified fluid has a density profile of the form

$$\rho_{total} = \rho_0 + \overline{\rho}(z) + \rho',$$

$$\overline{\rho}(z) = 28. - \gamma e^{z/1000},$$

$$\rho'(z) = 0.1 e^{z/1000} \quad kg \ m^{-3},$$

where $\rho_0 = 1000$kg m^{-3} and $\gamma = 3$ kg m^{-3}. The degree of stratification is quantified by the Burger number

$$S = \frac{N^2 H^2}{f_0^2 l^2} \approx 9.4,$$

where $N^2 = -g\delta_z\rho/\rho_0 H$, and H is the maximum water depth. As in Beckmann and Haidvogel (1993), the quantity $\rho_0 + \overline{\rho}(z)$ is treated as a known horizontally uniform background density

12

stratification which is removed prior to calculating the pressure gradient. The isopycnal disturbance ρ' is also horizontally uniform, but throughout the integration it is treated as a local density perturbation which is not removed prior to calculating the pressure gradient. The model starts from a state of rest with no surface forcing. Constant horizontal and vertical viscosities of 500 and 10^{-3} m^{2}s^{-1} are used, respectively. The boundary conditions are free-slip and the bottom friction is formulated linearly ($= r\mathbf{u}$ with r$=10^{-4}$ m s^{-1}). The horizontal and vertical diffusivities are both zero.

The model is run for 30 days with three different formulations: uniformly spaced σ-coordinates with the standard Jacobian pressure gradient formulation, and s-coordinates with $\theta = 3$ with both the standard and weighted Jacobian formulations. For the uniformly spaced σ-coordinate system with the standard Jacobian formulation, the peak velocity is 0.0005 m s^{-1}. This value is less than the values of 0.012 m s^{-1} (Fig. 6a, time series) and 0.001 m s^{-1} (Fig. 8, 4th order – medium stratification case) obtained respectively in the tests of Beckmann and Haidvogel (1993) and McCalpin (1995). If we improve the near surface resolution by choosing $\theta = 3$ (still using the standard Jacobian formulation), the peak velocity is reduced to 0.0003 m s^{-1}. If we use the weighted Jacobian formulation, we obtain the results shown in Fig. 1 for velocity u, v, w, and density change relative to the initial conditions through the center of the seamount. The magnitude of the peak velocity is about 0.0001 m s^{-1} at day 30 and has changed little since day 10 as shown in Fig. 1a and Fig. 1b. The density change in sigma-t units between day 30 and day 0 is 0.00032 as shown in Fig. 1d. This error is only slightly less than that obtained with uniformly spaced sigma levels, and either result is clearly acceptable for realistic oceanographic applications.

These results add support to the contention that the new pressure gradient schemes, in combination with the general vertical coordinate, can accurately represent the combined effects of steep topography ($\delta_x h/\delta x \approx 0.096$) and strong stratification ($S = 9.4$). Even in the case of sigma coordinates in combination with the standard Jacobian formulation, in which the hydrostatic consistency condition is strongly violated, results are acceptable for most applications.

We now use this problem to test the momentum consistency of the pressure gradient scheme, for which analytical considerations were presented in section 2. To do so, we calculate the line integral of the vertically averaged velocity along a contour of constant depth

$$LV_r = \frac{1}{2\pi r} \oint_{C_r} \overline{\mathbf{v}} \cdot \mathbf{t} \, dl, \tag{3.1}$$

and compare it to the mean speed along the same contour,

$$MV_r = \frac{1}{2\pi r} \oint_{C_r} \overline{\|\mathbf{v}\|} \, dl, \tag{3.2}$$

where $\overline{\mathbf{v}}$ is the vertically averaged velocity and $\|\mathbf{v}\|$ is the L_2 norm of $\mathbf{v}$, C_r is the depth contour at radius r from the center of the seamount, and $\mathbf{t}$ is the unit tangent vector along C_r. Results for LV_r and MV_r are plotted in Figs. 2a and b as functions of time for $r = 40$ and 80 km. The maximum value of LV_r/MV_r is less than 5×10^{-4}, which is not significantly different from zero if errors in estimating these quantities are taken into account. There are two separate factors which contribute to LV_r being slightly different from zero. First, the discrete representation of a line integral around a circular contour introduces some error. Second, the free surface in our model makes a fixed radius only an approximation to either a contour of constant depth or constant bottom pressure. Nevertheless, these results show that the pressure gradient force generates insignificant vertically integrated circulation along a contour of constant bottom depth compared to the mean current speed around the same contour.

Finally, we note that the values of MV_r illustrated in Fig. 2 reflect the erroneous velocity along the circle C_r, and LV_r is the corresponding net momentum generated by the pressure gradient error. Since the pressure gradient errors satisfy our numerical scheme, $LV_r \ll MV_r$ is expected for them just as for any other pressure driven flow.

3.2 A Test Basin

An unforced basin is now considered in order to directly compare with the results of MEO. This test is of special interest since the pressure gradient formulation used by MEO is very similar to our standard Jacobian formulation for the special case $\theta = 0$ (the σ-coordinate

14

system). The model domain has a continental shelf/slope on each wall of a periodic channel, which is equivalent to the two-dimensional case used in MEO. The width of the channel is 800 km with 41 grid nodes. The analytical form of the topography is

$$h(x) = h_{min} + (h_{max} - h_{min}) e^{-(r/l)^8}$$

where $h_{min} = 100$ m, $h_{max} = 4000$ m, $r = x - L/2$, $l = 3L/8$, and $L = 800$ km.

Following MEO, we initialize the model with the density,

$$\rho = 1028 - 3e^{z/1000}, \tag{3.3}$$

which is a reasonable approximation to the area-averaged, vertical distribution of the density in the North Atlantic Ocean. In contrast with the seamount test problem, the reference state $\bar{\rho}(z)$ is not subtracted prior to the pressure gradient calculation (this would give precisely the null solution). Constant horizontal and vertical viscosities of 2000 and 1×10^{-3} m^{2}s^{-1} are used. The horizontal and vertical diffusivities are both zero and there is no surface forcing.

The model is run diagnostically for 90 days, then prognostically for another 270 days. Results for along-shore velocity u and cross-shore pressure gradient errors across the basin at day 90 (the end of the diagnostic integration) are plotted in Figs. 3a and b, respectively. After 90 days of diagnostic integration, the magnitude of the peak velocity is about 0.04 m s^{-1}, of the same order as, but somewhat less than the peak value of order 0.07 m s^{-1} obtained by MEO. This error is generated by the pressure gradient force shown in Fig. 3b, which persists throughout the diagnostic integration. After day 90, we switch to prognostic integration and the peak velocity decreases rapidly, reaching about 0.002 m s^{-1} by day 270, as shown in Fig. 4a. This error is similar to that reported by MEO for day 270 of their model run and is negligible for most applications. During the prognostic integration, the density field is changed only slightly near the boundaries with weak upwelling associated with the clockwise circulation in the surface layers driven by the pressure gradient error (Fig. 4b). The maximum density change relative to initial conditions is -0.016 σ_t units, compared to 0.07 σ_t units reported by MEO. It is interesting to note that the ratio of our maximum density error

to that of MEO's is about 0.23 whereas the corresponding ratio of velocity errors is about 0.57. Using the thermal wind relation, this difference is consistent with the spatial scales of the errors in the present model being about 2.5 times smaller than those in MEO's model.

A important point to note is that the systematic errors in estimating horizontal gradients in the presence of a topography-following coordinate system, result in the model "seeing" erroneous isopycnal slopes in the initial state which actually has flat isopycnals ($\rho_{init} == \bar{\rho}(z)$). These erroneous isopycnal slopes correspond to an "error density field" which has potential energy associated with it, and this erroneous potential energy can actually dominate the erroneous kinetic energy that has received much more attention.

The model rest state ($\rho_{rest}(x, y, z)$) is achieved when the real isopycnals are tilted so as to cancel the error field, and can be determined simply by allowing the currents to spin down under the influence of bottom friction. Note that the final rest state does not depend on the details of the spin-down procedure; it is simply the state for which real pressure gradients due to tilting isopycnals balance the erroneous pressure gradients associated with the numerical scheme. As the model relaxes to this rest state, potential energy is released from the error density field and transformed into kinetic energy where it is dissipated. To illustrate this point, we have calculated the kinetic energy and potential energy referenced to the the density field ρ_{end} at the end of our model run (day 360), which we use as our best approximation for ρ_{rest}. Note that MEO also reference their potential energy to the end state of their model run, presumably for the same reason as it is done here.

The spatially averaged kinetic and potential energies (cm^2s^{-2}) relative to the end state are plotted for the diagnostic spin-up and prognostic continuation in Fig. 5a. The early stages of the diagnostic run are dominated by a kind of geostrophic adjustment in which the density field is kept fixed and only the velocity field adjusts. The kinetic energy increases rapidly during the first few hours as the velocity adjusts to the erroneous pressure gradients. During the next few days, the kinetic energy decreases slightly and the changes over the remaining 90 days are smaller yet. In contrast with our results, MEO find that their kinetic energy

decreases significantly during the initial 90 days of their diagnostic integration. However, even at the end of this period, the kinetic energy remains close to 1.5 cm^{2}s^{-2} which is much larger than the 0.18 cm^{2}s^{-2} achieved after just a few days of integration in the present case. Our results for this example remain similar (both qualitatively and quantitatively) whether we use s-coordinates or σ-coordinates and whether we use the standard Jacobian formulation or the weighted Jacobian formulation. It is noteworthy that the increased total KE seen in the MEO results in comparison with the present results is again consistent with larger spatial scales for the error fields in the MEO results. Based on the ratio of maximum error velocities (≈ 1.75) and the previously mentioned ratio of horizontal scales (≈ 2.5), we might expect MEO's total KE to be approximately 7.7 ($\approx 2.5 \times 1.75^2$) times our values, which is encouragingly consistent with the value of 8.3 obtained from detailed calculations.

It should be noted that the changes in total energy during diagnostic integration do not violate any principles of energy conservation. Immediately after the run is initiated, potential energy is converted to kinetic energy which is then subject to dissipation. The kinetic energy is continuously renewed from the potential energy pool which is maintained at its initial level by the specification of the density field. The unspecified buoyancy sources which maintain the density field also balance the energy budget.

Under prognostic integration, our model currents decrease abruptly, consistent with the "advective elimination" of the pressure gradient error discussed by MEO. However, the error decreases much more abruptly in the present case. After 180 days of prognostic integration, both the potential and kinetic energies are very small (2.24×10^{-6} and 2.25×10^{-6} m^{2}s^{-2}, respectively). For horizontal viscosity of 2000 m^2 s^{-1}, the decay time of order ten days implies a horizontal length scale of order 50 km which is in reasonable agreement with the scales seen in Fig. 5a. Additional calculations reveal that the damping associated with vertical variations makes a smaller, but still significant contribution. Note that the more rapid spin down evident from comparison of Fig. 5a with MEO's Fig. 3 is again consistent with the smaller spatial scales of the error field obtained from the present calculation. Thus, the main differences between our results and MEO's apparently reflect the larger spatial scale

17

of the errors obtained by MEO. The precise reason for the difference in spatial scales remains unknown.

In order to further verify the consistency of the pressure gradient scheme, we have calculated the net energy conversion term in the KE equation:

$$VGP = -\iiint_V \mathbf{v} \cdot \nabla p \, dv, \tag{3.4}$$

and compared it to the corresponding energy conversion term in the potential energy equation:

$$PEtoKE = -\frac{g}{\rho_0} \iiint_V \rho' w \, dv. \tag{3.5}$$

VGP is the volume integral of the first term of equation (2.17) and $PEtoKE$ is minus the volume integral of the first term on the right of (2.18). VGP must balance $PEtoKE$ in order to guarantee energy consistency, and the analytical results presented in section 2, indicate that this should be true

Fig. 5b shows the time integral of VGP, $KEtoPE$ (solid lines), and $PEtoKE$ (dashed lines) as functions of time, starting from day 90. As expected, VGP is almost equal to $PEtoKE$. Indeed, the agreement is excellent, given that our analytical proof was for the semi-discrete equations. The equivalence of these two curves (to the accuracy that we can calculate them) confirms that the numerical representations of the energy conversion terms in the kinetic and potential energy equations are consistent.

Finally, we offer the following physical discussion of the "advective elimination" of the pressure gradient error proposed by MEO. When starting the prognostic integration from day 90, the model "sees" an initial state with erroneous horizontal isopycnal slopes, i.e., the initial pressure gradient error as plotted in Fig. 3b. Due to this erroneous force, a current field develops which, due to viscous dissipation, tends to relax to a rest state, for which the real isopycnal slopes counter the error slopes. During the relaxation, the potential energy stored in the original error buoyancy field is effectively converted to kinetic energy as required for energetic consistency ($VGP = PEtoKE$). After conversion to kinetic energy, the energy is dissipated by viscous effects. It is important to realize that the error field is governed by the

18

finite difference equations and hence satisfies the conditions for energetic consistency, just as the total fields do, as required for the success of long term integrations (Arakawa and Lamb, 1977).

4 Performance in Forced Examples

In the previous section, two unforced test cases were considered in order to evaluate the influence of the pressure gradient error under the simplest possible conditions. The results clearly indicate that the new formulations of the pressure gradient warrant further investigation. This section is intended to investigate the performance of the formulations in somewhat more realistic examples for which analytical solutions are not available, but qualitative features are known from previous studies.

We consider the classical problem of determining the circulation in a rectangular, mid-latitude basin driven by a double-gyre wind stress field. The computational domain is 3600 km by 2800 km. A grid of 180×140 cells is used (20 km resolution) for eddy-permitting (but not fully resolving) resolution. There are 20 vertical levels and we use Song and Haidvogel's (1993) s-coordinate system with $\theta = 3$. The background stratification (i.e., the initial buoyancy field) is given by

$$\bar{\rho}(z) = \rho(z, t = 0) = 28 - 5.8039 \exp(z/800)[0.6 - 0.4 \tanh(z/800)],$$

and the model is started from a state of rest. The β-plane approximation,

$$f = f_0 + \beta y \ ,$$

is used with $f_0 = .9 \times 10^{-4}$, $\beta = 2 \times 10^{-11}$, and $y = 0$ is at the center of the domain. The driving force is provided by a double-gyre wind stress field,

$$\tau^x = 1 \times 10^{-4} \cos(2\pi y/L_y), \qquad \tau^y = 0,$$

where L_y is the north-south extent of the basin. In the following experiments, constant lateral and vertical viscosities of 300 and 1×10^{-3} m^{2}s^{-1} and diffusivities of 100 and 1×10^{-4} m^{2}s^{-1}

are used, respectively. The momentum boundary condition is free-slip and the bottom friction is formulated linearly with drag coefficient 1×10^{-4} m s^{-1}.

Based on the above model configuration, we conduct two experiments, one with a flat bottom and the other with a slope region on the western side of the basin. Although we cannot quantify the pressure gradient errors in these cases, verification of the expected qualitative behavior is essential in testing the performance of the numerical schemes for use in long-term integration of large-scale problems. We expect the ocean to develop a double-gyre circulation with a western boundary current which should separate from the boundary and shed eddies and rings as it extends across the basin (Haidvogel et al. 1992, McWilliams and Gent 1994). We note that even this simple problem has not previously been investigated in a free surface, generalized topography-following coordinate model.

Experiment A: With A Flat Bottom

In our first experiment, the bottom is flat and at a depth of 5000m. In this case, the model is essentially a free-surface z-coordinate model because the constant s levels very nearly coincide with constant z levels (there is a slight difference due to the fact that $s = 0$ follows the free surface). In addition to testing the stability of the numerical scheme, this experiment demonstrates how the free-surface model performs in a simulation which includes strong boundary currents and an internal jet, a demonstration which has not been shown previously.

The model is run prognostically for 10 years and the velocity and density fields at about 100 meter depth, at the end of the run, are shown in Fig. 6. Similar to the results reported by Haidvogel et al. (1992), in their free-slip boundary condition case, the western boundary current separates at or near the center of the domain, where the wind stress curl is zero and the current meanders to the east. Cold cyclonic eddies and warm anticyclonic eddies are detached from the south and north sides of the zonal jet, respectively (Spall and Robinson, 1990). The zonal transport stream function is given in Fig. 7a and the meridional transport streamfunction is given in Fig. 7b. The zonal circulation shows a concentrated cell with eastward surface flow near the western boundary, above approximately 500 m depth. The

maximum transport is approximately 6 Sv, and the eastward flow extends from the western boundary to the center of the basin above about 500 meter depth. The meridional overturning circulation shows a three-cell pattern: a broad sinking cell at the northern boundary of about 4 Sv; a similar upwelling cell at the southern boundary; and a concentrated, narrow umbrella-like cell at the center of the domain of about 3 Sv. These results are generally consistent with expectations based on previous studies such as Holland (1978) and McWilliams et al. (1990).

Experiment B: With A Western Slope

In our second experiment, a continental slope is added to the western side of the basin. No other changes are made. The bottom depth varies only in the east-west direction, with a narrow western shelf at a depth of 1200 meters, a broad continental slope region about 500 kilometers wide, and a deep basin with constant depth of 5000 meters as in the flat bottom case.

The model is again run prognostically for 10 years and the final velocity and density fields at about 100 meters depth are shown in Fig. 8. As expected, cold cyclonic eddies and warm anticyclonic eddies still detach from the south and north sides of the boundary currents, similar to the flat bottom case. However, the separation latitude of the western boundary current shifts south of the zero wind stress curl line by about 500 km and a wedge of northern water is advected further southward along the slope. The zonal transport stream function is given in Fig. 9a and the meridional transport streamfunction is given in Fig. 9b. The maximum transports associated with both zonal and meridional circulations are substantially enhanced compared to the flat bottomed case. Although the near-surface eastward transport is about the same as in the flat bottom case, there is a strong eastward transport near the bottom over the lower slope increasing to 11 Sv. These values are nearly twice the corresponding values for the case with no topography. In the meridional overturning circulations, the three-cell pattern in the flat bottom case no longer exists, being replaced by two larger cells, a broad enhanced sinking at the northern boundary of about 8 Sv, which is twice that found in the flat bottom experiment, and a concentrated downwelling cell at the southern boundary of

about 30 Sv, which is about 10 times the maximum overturning transport in the flat bottom case. Note that the enhanced transports are concentrated over the continental slope in the southern part of the basin.

From these results, it is clear that the sloping topography plays an important role in the basin-scale circulations considered here. Perhaps the most obvious effects of the sloping topography are the southward advection of a wedge of northern water and the earlier separation of the northward flowing western boundary current. According to the results of Myers et al. (1996), these two effects are causally related through the JEBAR term.

Another obvious influence of the sloping topography is the enhancement of both zonal and meridional overturning transports. By analyzing a simplified depth-integrated steady-state vorticity equation, Holland (1973) describes the physical mechanics responsible for the enhanced transports. In our eddy-resolving simulation, the basin-scale circulation has not reached steady state, but after ten years of integration it approaches a statistically steady state.

We now determine a quantitative estimate of the bottom pressure torque effect in order to confirm its importance in determining the differences in the circulations seen in our two experiments. The vertically integrated vorticity equation can be obtained by taking the curl of the momentum equations for the vertically averaged velocity components. The resulting equation can be written as

$$
\begin{aligned}
\frac{\partial}{\partial t}\left[\frac{\partial \bar{v}H}{\partial x} - \frac{\partial \bar{u}H}{\partial y}\right] = & \frac{\partial p_b}{\partial x}\frac{\partial H}{\partial y} - \frac{\partial p_b}{\partial y}\frac{\partial H}{\partial x} \\
& - \frac{\partial(f\bar{u}H)}{\partial x} - \frac{\partial(f\bar{v}H)}{\partial y} \\
& + \frac{\partial AD_y}{\partial x} - \frac{\partial AD_x}{\partial y} \\
& + \frac{\partial(\tau_s^y - \tau_b^y)}{\partial x} - \frac{\partial(\tau_s^x - \tau_b^x)}{\partial y} \, ,
\end{aligned}
\tag{4.6}
$$

where $\bar{u}$ and $\bar{v}$ are the vertically averaged velocity components, $H = \zeta + h$ is the total water depth, AD_x and AD_y are the horizontal advection and diffusion terms, p_b is the dynamic bottom pressure, (τ_s^x, τ_s^y) and (τ_b^x, τ_b^y) are the surface and bottom stress terms, respectively.

For steady-state flow, or under the rigid lid approximation, the term containing the Coriolis parameter reduces to $-\beta \bar{v} H$, where $\beta = df/dy$.

The importance of the bottom pressure torque is most easily revealed by examining the vorticity balance at a latitude removed from intense eddy activity. Fig. 10 shows the zonal distributions of vorticity terms at the latitude of the maximum (negative) wind-stress curl, about 700 km south of the basin center, for the two basin circulations. Only results for the western half of the basin (out to 1800 km from the western boundary) are plotted. The vorticity tendency and the surface and bottom stress terms are relatively small in both cases and are not shown. In the flat bottom case (Fig. 10a), the bottom pressure torque (dashed line) vanishes and the Coriolis term (solid line) is is very nearly balanced by the advection and diffusion term (dash-dot line). The maximum (negative) value of the Coriolis term near the western boundary reflects the strong northward transport (i.e., $-\beta \bar{v} H < 0$) within the Munk boundary layer.

With the effect of a slope region included along the western boundary, these features are significantly modified (Fig. 10b). The maximum values of the vorticity terms shift 600 km offshore to the slope region. The bottom pressure torque (dashed line) is dominant in this region and is in approximate balance with the Coriolis term (solid line), with a smaller contribution from the advection and diffusion term (dash-dot line). The individual terms in the vorticity balance are three times bigger than those in the flat bottom case.

In each of these model runs, the wind stress is the only external force driving the fluid. However, as Holland (1973) points out, the dynamical balance is strongly modified by the presence of topography. In particular, the stretching of vortex tubes associated with the bottom velocity can be large: a horizontal velocity as small as 0.1 ms^{-1} perpendicular to a continental slope with gradient 10^{-3} is able to produce a depth integrated torque comparable to that associated with a typical wind stress curl. In our second experiment, a maximum slope of 2% has been used, which is typical of the mean slope off the west coast of North America. With this slope, we find that the bottom torque is up to 10 times the magnitude of

the driving wind stress curl.

In summary, our flat-bottomed experiment illustrates that the model is stable and capable of resolving the evolution of the western boundary current along with its associated eddy activity. In this case, there is effectively no pressure gradient error associated with the use of *s*-coordinates since the *s* levels nearly coincide with constant *z* levels. In our second experiment, a mean slope typical of that off the west coast of North America is included. The success of this experiment, using the same parameters and time-step as in the flat bottom case, indicates that any errors due to the coordinate transformation have not caused serious numerical problems. It also indicates, at least qualitatively, that the proposed pressure gradient schemes are able to handle the slopes and bottom torques present in the regions of strong western boundary currents. Finally, our results are at least qualitatively consistent with earlier work (Holland 1973, Myers et al. 1996) suggesting that the sloping topography plays a dominant role in the enhanced circulations and earlier separation of the Gulf Stream due to the joint effect of baroclinicity and relief (JEBAR).

5   Summary and Conclusions

The difficulty in handling the interaction of sleep topography with boundary currents and eddies in numerical ocean models is well known (e.g., Gerdes, 1993). Correctly representing the JEBAR contribution to the bottom torque is particularly challenging with topography-following coordinates due to the fact that this contribution is largest where there is a combination of steep topography and strong stratification (Beckman and Haidvogel, 1993).

To improve the simulation of oceanic flow with numerical models using topography-following coordinate systems, Song (this issue) introduced two general pressure gradient formulations. These formulations are based on integrating the Jacobian of density and vertical coordinate to obtain a discrete representation of the horizontal pressure gradient at any given level. The standard Jacobian formulation is based on centered differences in the computa-

tional s-coordinate system while the weighted Jacobian formulation uses a particular vertical weighting such that the buoyancy gradient estimates are effectively centered in the more usual z-coordinate space. Both schemes are general, can be used with any vertical coordinate system (see Part I) and are easily implemented.

To further understand the behavior of the proposed pressure gradient schemes, we have investigated the integral properties of the schemes. In each case, a combination of theoretical and numerical analyses have been used to demonstrate the properties of the schemes.

The particular integral properties considered here are the conservation of momentum and energy and the accurate representation of the bottom pressure torque. The validity of the first two properties has been illustrated for two unforced test examples involving steep slopes and isolated topographic features in the presence of strong stratification. All tests are carried out with a general vertical coordinate model (SCRUM) which allows us to examine the performance in both the σ-system and the s-system. Our results confirm that pressure gradient errors associated with the use of topography-following coordinates may be substantially reduced through the choices of the numerical scheme and coordinate system.

The performance of the schemes in long-term integrations has been evaluated using double-gyred wind-forcing of a large scale basin, both with and without a continental slope on the west side of the basin. The model is run for 10 years in each case and it generates realistic western boundary currents and detached eddies. By comparing results from these two experiments, we find that the presence of the topography results in a southward shift of the separation latitude for the model Gulf Stream. Our results are consistent with Holland's (1973) conclusion that the bottom pressure torque contributes significantly to the vorticity balance, resulting in enhancement of the western boundary current, and with Myers et al.'s (1996) conclusion that changes in JEBAR have an important influence on the separation of the Gulf Stream.

The difficulty, mainly due to pressure gradient errors (Deleersnijder and Beckers, 1992), in representing the combined effects of steep topography and strong boundary currents in topography-following coordinate models has been recognized for many years. The poor rep-

resentation of sloping topography in z-coordinate models is also well-known (Gerdes, 1993). Each of these model shortcomings have the potential to result in substantial errors in the representation of the bottom torque, which is a critical aspect of ocean dynamics. Our findings indicate that, at least with the pressure gradient formulations considered here, models using topography-following coordinates can reasonably represent the bottom pressure torque. For either type of coordinate system, special care should be taken with regard to this issue. Additional tests in more realistic applications are still clearly required.

References

[1] Arakawa, A., and V. R. Lamb, 1977: Computational design of the basic dynamic processes of UCLA general circulation model, in *Methods in Comput. Phys.*, (Academic Press, New York/London, 1977), **17**, 173.

[2] Arakawa, A. and M. J. Suarez, 1983: Vertical differencing of the primitive equations in Sigma Coordinates, *Mon. Wea. Rev.*, **111**, 34-45.

[3] Arakawa, A. and C. S. Konor, 1996: Vertical differencing of the primitive equations on the Charney-Phillips grid in hybrid $\sigma - p$ vertical Coordinates, *Mon. Wea. Rev.*, **124**, 511-528.

[4] Blumberg, A. F., and G. L. Mellor, 1987: A description of a three-dimensional coastal ocean circulation model, *Three-dimensional Coastal Ocean Models*, N. Heaps, Ed., American Geophysical Union, Vol. 4, 208 pp.

[5] Bechmann, A., and D.B. Haidvogel, 1993: Numerical simulation of flow around at al isolated seamount, Part I: problem formulation and model accuracy, *J. Phys. Oceanogr.*, **23**, 1736-1753.

[6] Bleck, R., 1978: Finite difference equations in generalized vertical coordinates. Part I: total energy conservation, *Contrib. Atmos. Phys.*, **51**, 360-372.

[7] Bryan, K., 1969: A numerical method for the study of the circulation of the world ocean, *J. Comp. Phys.*, **4**(3), 347-376.

[8] Deleersnijder, E., and J.-M. Beckers, 1992: On the use of the σ-coordinate system in regions of large bathymetric variations, *J. Marine Sys.*, **3**, 381-390.

[9] Gent, P. R., 1993: The energetically consistent shallow-water equations, *J. Atmos. Sci.*, **50** (9), 1323-1325.

[10] Gerdes, R., 1993: A primitive equation ocean circulation model using a general vertical coordinate transformation, I. Description and testing of the model, *J. Geophy. Res.*, **98** (C8), 14,683-14,701.

[11] Greatbatch, R. J., A. F. Fanning, A. D. Goulding, and S. Levitus, 1991: A diagnosis of interpentadal circulation changes in the North Atlantic, *J. Geophys. Res.* , **96**, 22009-22023.

[12] Haidvogel, D.B., J.C. McWilliams and P.R. Gent, 1992: Boundary current separation in a quasi-geostrophic, eddy-resolving ocean circulation model. *J. Phys. Oceanogr.*, **22**, 882-902.

[13] Haney, R. L., 1991: On the pressure gradient force over steep topography in sigma coordinate ocean models, *J. Phys. Oceanogr.*, **21**, 610-619.

[14] Holland, W. R., 1967: On the wind-driven circulation in an ocean with topography, *Tellus* XIX, **4**, 582-599.

[15] Holland, W. R., 1973: Baroclinic and topographic influences on the transport in western boundary currents, *Geophys. Fluid Dyn.*, **4**, 187-210.

[16] Holland, W. R., 1978: The role of mesoscale eddies in the general circulation of the ocean – numerical experiments using a wind-driven quasi-geostrophic model. *J. Phys. Oceanogr.*, **8**, 363-392.

[17] Kasahara, A., 1974: Various vertical coordinate system used for numerical weather prediction, *Mon. Wea. Rev.*, **102**, 509-522.

[18] McWilliams, J.C., N.J. Norton, and P.R. Gent, 1990: A linear balance model of the wind-driven, midlatitude ocean circulation. *J. Phys. Oceanogr.*, **20**, 1349-1378.

[19] Mellor, G.L., C.R. Mechoso, and E. Keto, 1982: A diagnostic calculation of the general circulation of the Atlantic Ocean. *Deep Sea Research*, **29**, 1171-1192.

[20] Mellor, G.L., T. Ezer, and L.-Y. Oey, 1994: The pressure gradient Conundrum of sigma coordinate ocean models, *J. Atmos. Ocean Tech.*, **11**(4), 1126-1134.

[21] Mertz, G., and D. G. Wright, 1992: Interpretations of the JEBAR term, *J. Phys. Oceanogr.*, **22**, 301-305.

[22] Myers, P. G., A. F. Fanning, and A. J. Weaver, 1996: JEBAR, bottom pressure torque and Gulf Stream Separation, *J. Phys. Oceanogr.*, **26**, 671-683.

[23] Sarkisyan, A. S., and V. F. Ivanov, 1971: Joint effect of baroclinicity and bottom relief as an important factor in the dynamics of sea currents, *Izv. Acad. Sci. USSR Atmos. Oceanic Phys., Engl. Transl.*, **7**, 173-178.

[24] Simmons, A. J., and D. M. Burridge, 1981: An energy and angular momentum conserving vertical finite difference scheme and hybrid vertical coordinates, *Mon. Wea. Rev.*, **109**, 758-766.

[25] Spall, M. A., and A. R. Robinson, 1990: Regional primitive equation studies of the Gulf Stream meander and ring formation region, *J. Phys. Oceanogr.*, **20**, 985-1016.

[26] Song, Y., 1996: User's manual for the S-coordinate Rutgers University Model, *Tech. Report*, pp 48.

[27] Song, Y. and D. Haidvogel, 1994: A semi-implicit ocean circulation model using a generalized topography-following coordinate system, *J. Comput. Physics*, **115** (1), 228-244.

[28] Yingshuo, S., and K. Thompson, 1997: Oscillating flow of a homogeneous fluid over an isolated topographic feature, *Atmosphere-Ocean*, **35**, 229-255.

Figure Captions

Figure 1: Cross sections through the center of the seamount: a) the along-shore velocity; b) the cross-shore velocity; c) the vertical velocity; d) the density change relative to the initial conditions. Units are in $m\ s^{-1}$ for u, v, w, and in $kg\ m^{-3}$ for ρ.

Figure 2: a) Line integral of vertically averaged velocity and b) mean velocity along seamount isobaths as a function of time (in days), where $r1 = 40km$ and $r2 = 80km$ are the radii of isobaths of the seamount.

Figure 3: Cross sections through the center of the basin after the 90 day diagnostic run: a) the along-shore velocity ($m\ s^{-1}$) and b) the cross-shore pressure gradient errors.

Figure 4: a) The along-shore velocity ($m\ s^{-1}$) and b) the density change relative to initial conditions (sigma-t units) after continuing the run of Fig. 3 for another 180 days prognostically.

Figure 5: a) Spatially averaged kinetic energy and potential energy relative to the end state at 360 day as a function of time, b) the time integral of pressure gradient terms and PEtoKE terms as a function of time.

Figure 6: Results for the velocity field superposed on the density field at 10 years (3650 days) simulation of double-gyre wind-driven basin with flat bottom. Contour units are in sigma-t.

Figure 7: Transport streamfunctions corresponding to the end of a 10 years simulation of a double-gyre wind-driven basin with flat bottom, a) zonal transports and (b) meridional transports. Contour units are in Svertrup ($10^6 m^3 s^{-1}$).

Figure 8: Same as Fig. 6, but with the effect of a western slope included.

Figure 9: Same as Fig. 7, but with the effect of a western slope included.

Figure 10: The zonal distribution of terms in the right-hand-side of the vorticity equation (4.6) at the latitude of the maximum (negative) wind-stress curl, about 700 km south of the basin center. Only half of the western domain is plotted. The unites are $m\ s^{-2}$.

a). U(XI = 20,DAY = 30.0)

CONTOUR FROM -.0000275 TO .0001075 BY .000005

b). V(XI = 20,DAY = 30.0)

CONTOUR FROM -.000085 TO .000085 BY .00001

c). W(XI = 20,DAY = 30.0)

NTOUR FROM -.000003625 TO .000001125 BY .00000025

d). RHO(XI = 20,DAY = 30.0)
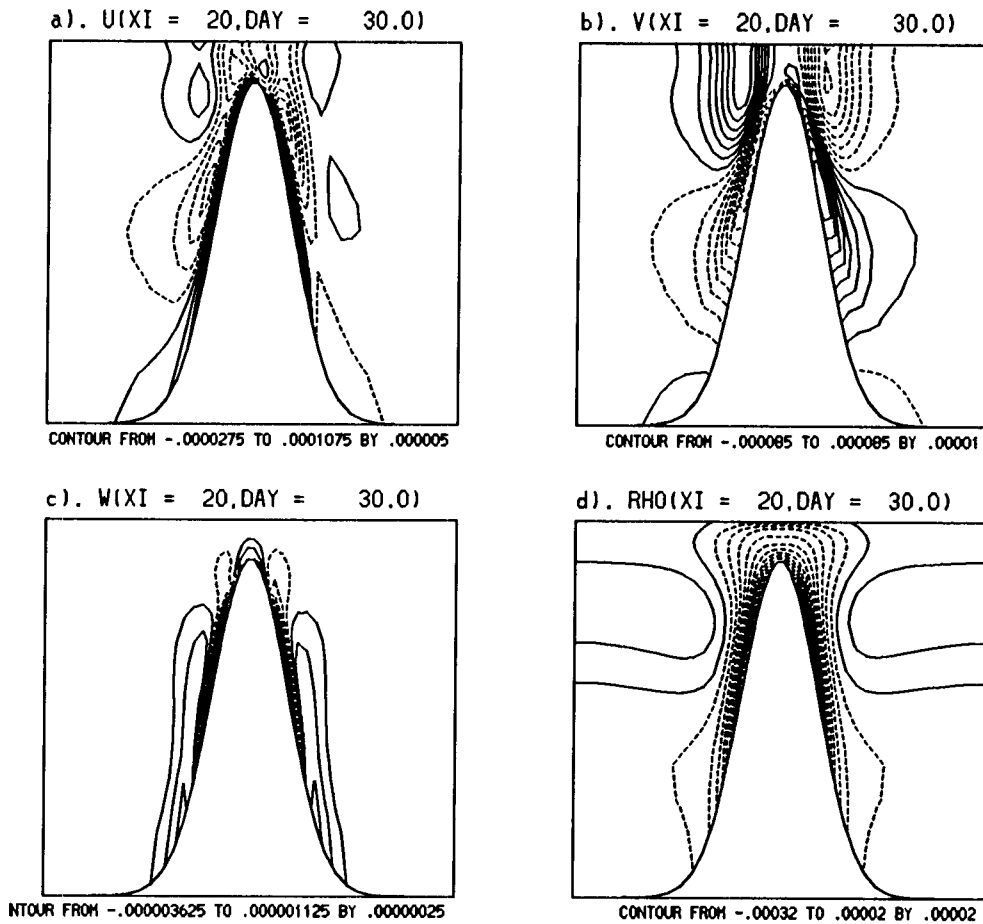
CONTOUR FROM -.00032 TO .00002 BY .00002

Figure 1: Cross sections through the center of the seamount: a) the along-shore velocity; b) the cross-shore velocity; c) the vertical velocity; d) the density change relative to the initial conditions. Units are in $m\ s^{-1}$ for u, v, w, and in $kg\ m^{-3}$ for ρ.
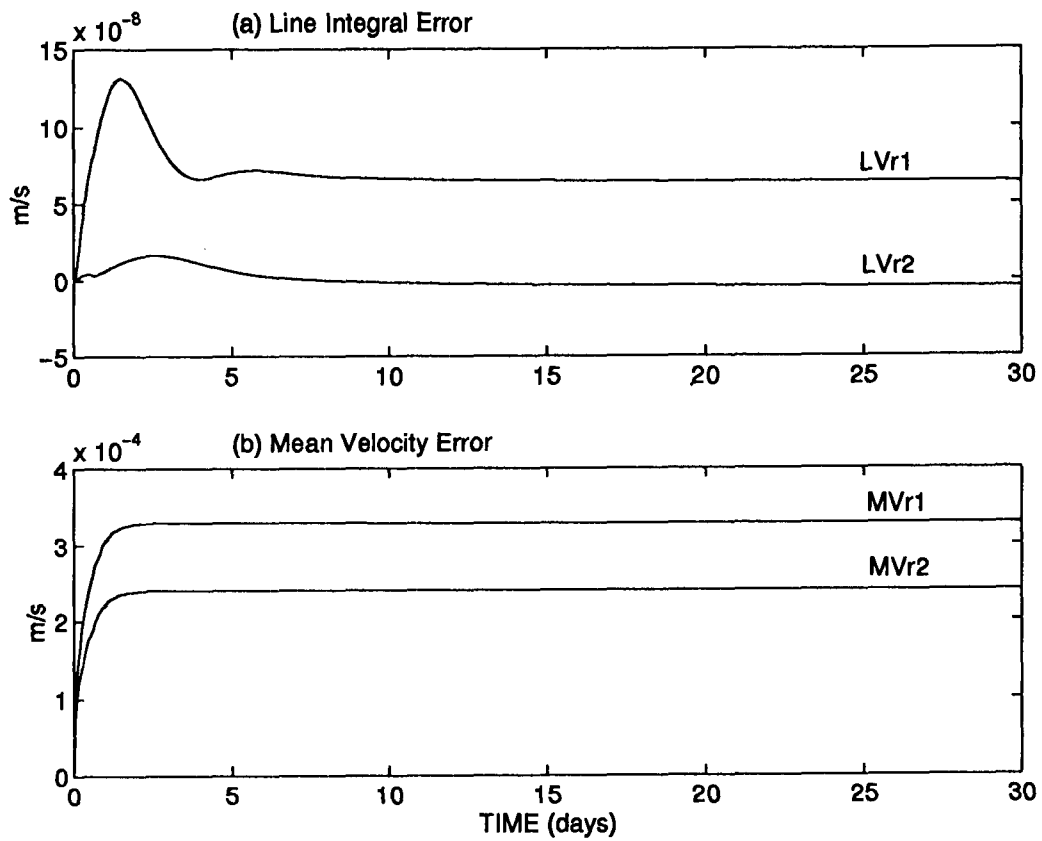
Figure 2: a) Line integral of vertically averaged velocity and b) mean velocity along seamount isobaths as a function of time (in days), where $r1 = 40km$ and $r2 = 80km$ are the radii of isobaths of the seamount.
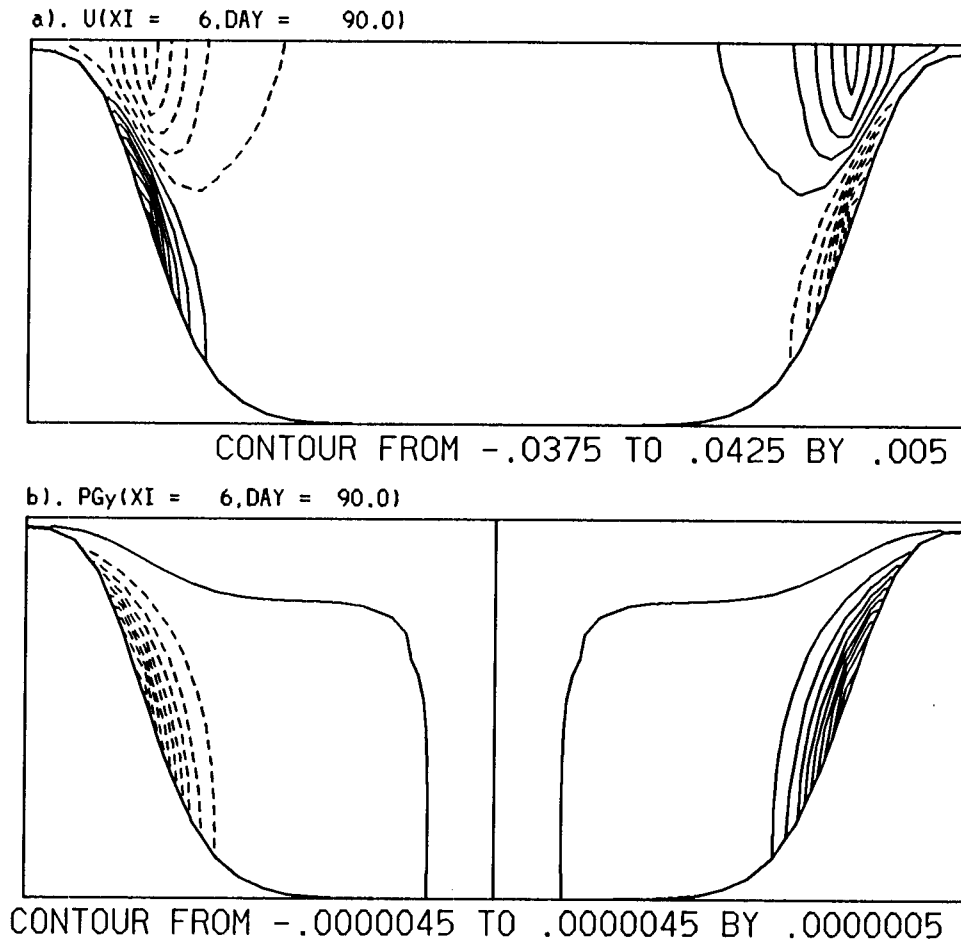
a). U(XI = 6,DAY = 90.0)

CONTOUR FROM -.0375 TO .0425 BY .005

b). PGy(XI = 6,DAY = 90.0)

CONTOUR FROM -.0000045 TO .0000045 BY .0000005

Figure 3: Cross sections through the center of the basin after the 90 day diagnostic run: a) the along-shore velocity (m s^{-1}) and b) the cross-shore pressure gradient errors.

33

a). U(XI = 6,DAY = 270.0)

CONTOUR FROM −.002375 TO .002625 BY .00025

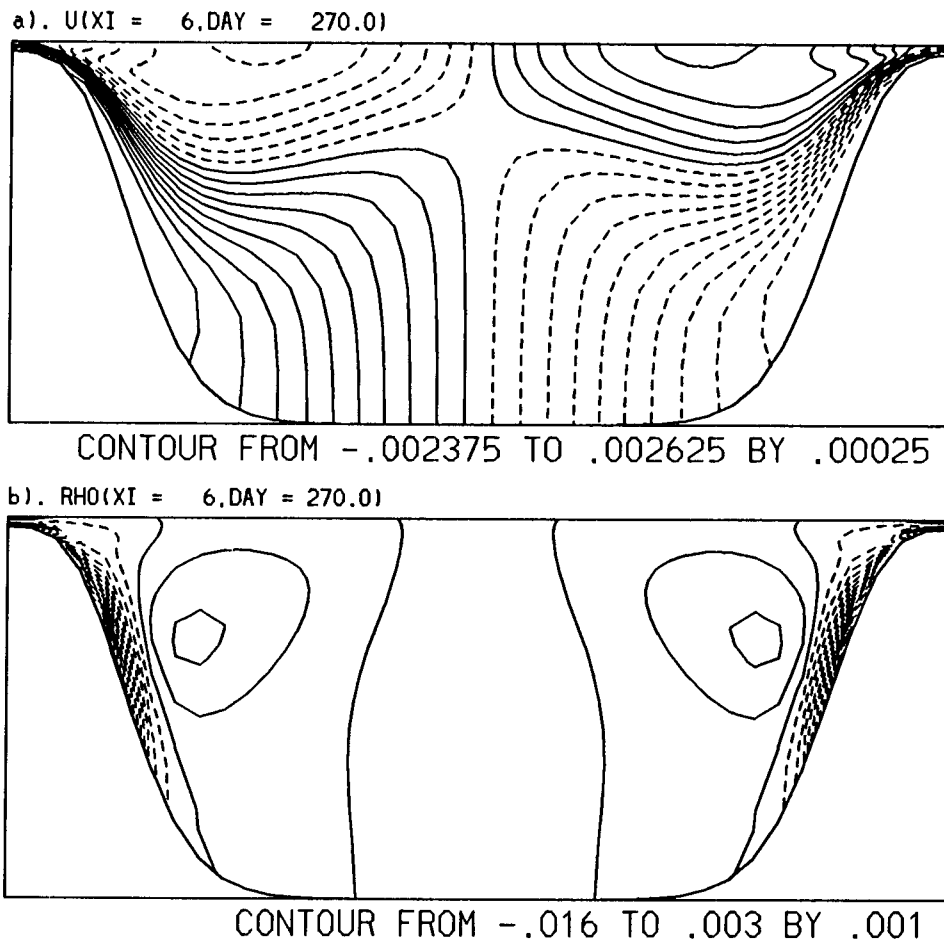b). RHO(XI = 6,DAY = 270.0)

CONTOUR FROM −.016 TO .003 BY .001

Figure 4: a) The along-shore velocity ($m\ s^{-1}$) and b) the density change relative to initial conditions (sigma-t units) after continuing the run of Fig. 3 for another 180 days prognostically.
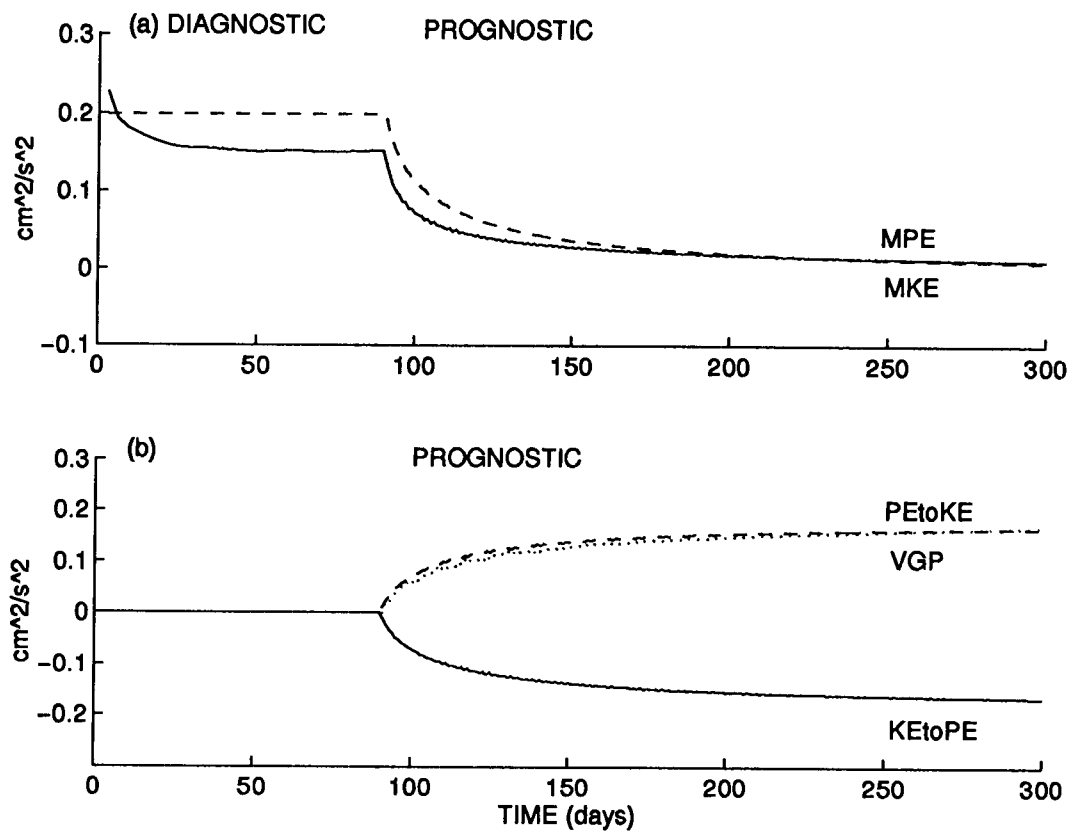
Figure 5: a) Spatially averaged kinetic and potential energies relative to the end state at 360 days as a function of time, b) the time integral of the pressure gradient term and PEtoKE term as functions of time.